Mapping the Relationship between Northern Hemisphere Winter Surface Air Temperature and the Madden–Julian Oscillation

YANG ZHOU

School of Atmospheric Sciences, Nanjing University, Nanjing, China

KEITH R. THOMPSON

Department of Oceanography, Dalhousie University, Halifax, Nova Scotia, Canada

YOUYU LU

Department of Fisheries and Oceans, Bedford Institute of Oceanography, Dartmouth, Nova Scotia, Canada

ABSTRACT

A regression-based modeling approach is described for mapping the dependence of atmospheric state variables such as surface air temperature (SAT) on the Madden–Julian oscillation (MJO). For the special case of a linear model the dependence can be described by two maps corresponding to the amplitude and lag of the mean atmospheric response with respect to the MJO. In this sense the method leads to a more parsimonious description than traditional compositing, which usually results in eight maps, one for each MJO phase. Another advantage of the amplitude and phase maps is that they clearly identify propagating signals, and also regions where the response is strongly amplified or attenuated. A straightforward extension of the linear model is proposed to allow the amplitude and phase of the response to vary with the amplitude of the MJO or indices that define the background state of the atmosphere–ocean system. Application of the approach to global SAT for boreal winter clearly shows the propagation of MJO-related signals in both the tropics and extratropics and an enhanced response over eastern North America and Alaska (further enhanced during La Niña years). The SAT response over Alaska and eastern North America is caused mainly by horizontal advection related to variations in shore-normal surface winds that, in turn, can be traced (via signals in the 500-hPa geopotential height) back to MJO-related disturbances in the tropics.

1. Introduction

The Madden–Julian oscillation (MJO) is the primary mode of variability of the tropical atmosphere on intraseasonal time scales (Madden and Julian 1971, 1972). The MJO has been related to a wide variety of atmospheric phenomena at low latitudes including the El Niño–Southern Oscillation (ENSO; e.g., Kessler and Kleeman 2000; McPhaden et al. 2006), the onset of the Indian monsoon (e.g., Lau and Chan 1986) and the East Asian monsoon (e.g., Wu and Zhang 1998), the North American monsoon system (Higgins and Shi 2001), and tropical cyclone activity (e.g., Kim et al. 2008; Camargo et al. 2008).

Previous work has shown that the MJO can affect intraseasonal variability in the extratropics. [See Madden and Julian (1994) for a discussion of the early work, and Zhang (2005) for a more recent review.] For example, Jones et al. (2004) pointed out that the MJO can modulate extratropical weather and can be used to improve extratropical weather forecasts. Pan and Li (2008) found that atmospheric heating associated with the MJO can excite a significant midlatitude response. There is growing evidence that the MJO is related to several modes of variability of the Northern Hemisphere atmosphere during winter. For example, Mori and Watanabe (2008) found that 30% of the temporal variability of the Pacific–North America pattern (PNA, which is an important mode of North American variability; e.g., Notaro et al. 2006) can be explained by the MJO. The MJO has also been shown to be related to the Arctic Oscillation (AO; Zhou and Miller 2005; L'Heureux and Higgins 2008)

Corresponding author address: Keith R. Thompson, Department of Oceanography, Dalhousie University, Halifax, NS B3H 4J1, Canada.
E-mail: keith.thompson@dal.ca

and the North Atlantic Oscillation (NAO; Cassou 2008; Lin et al. 2009). Vecchi and Bond (2004, hereafter VB04) showed that surface air temperature (SAT) for Alaska is related to the MJO during winter. The MJO has also been shown to have a significant influence on eastern North American SAT (Lin and Brunet 2009, hereafter LB09).

Both linear and nonlinear models have been used to explore the relationship between the MJO and extratropical atmospheric variations. Focusing first on dynamical studies we note that Winkler et al. (2001) used a linear model to show that the inclusion of tropical heating associated with the MJO can improve predictions of extratropical variability. Blade and Hartmann (1995) used a global two-level model to show that the MJO, through tropical heating, can have a nonlinear influence on extratropical intraseasonal variability. Turning to statistical studies we note that the compositing of observed atmospheric fields according to MJO phase has been used for many years to help identify the influence of the MJO on variables such as SAT (e.g., Jeong et al. 2005; VB04; LB09). Compositing is a flexible technique that imposes no constraints on the atmospheric state as the MJO changes from one phase to another. More recently Jamet and Hsieh (2005) have used neural networks to study the nonlinear influence of the MJO on precipitation and the 200-hPa wind in the northeastern Pacific during winter.

In this study, we explore the relationship between the MJO and changes in extratropical SAT using two complementary approaches. The first approach involves the development and implementation of a straightforward, statistically based method for mapping changes in the atmosphere associated with the MJO. The method is a modified form of compositing and can accommodate both linear and nonlinear relationships between the atmospheric variables of interest (e.g., SAT) and indices defining the MJO and the background state of the atmosphere and ocean. In the present study, we use the bivariate index (with components x_1 and x_2) of Wheeler and Hendon (2004, hereafter WH04). One of the advantages of the new method is that, in the linear case, the predicted atmospheric response can be described in terms of a spatially dependent amplitude and phase lag, similar to the cotidal and cophase maps used for many years by oceanographers to describe the spatial variation of sea level due to tides. We also extend the linear model to allow the predicted response to change nonlinearly with the amplitude of the MJO ($A = \sqrt{x_1^2 + x_2^2}$) and also indices describing the background state of the atmosphere and ocean (e.g., El Niño). The second approach is based on dynamics and is used to explain in physical terms the major features evident in the maps of atmospheric response to the MJO.

The structure of the paper is as follows. Section 2 describes the atmospheric observations and indices used in this study, and presents composites of boreal winter SAT calculated in the traditional way. The new method of estimating atmospheric response based on both linear and nonlinear models is described in section 3. The approach is applied to global observations of SAT in section 4. Consistent with previous analyses (e.g., VB04; LB09), we find the strongest SAT response over Alaska and eastern North America. Section 5 focuses on the physical reasons for the amplified SAT response in these two regions. Discussions and suggestions for further work are given in section 6.

2. Observations and composite analysis of surface air temperature

We first describe the fields of surface observations that will be related to the MJO, the indices used to modulate the response, and the temporal filtering of the data. This is followed by traditional compositing of SAT according to MJO phase. The composites are compared to results from the regression-based approach in subsequent sections.

a. Observations, indices, and filtering

The atmospheric "observations" to be related to the MJO consist of daily global fields of geopotential height (H_{500}), sea level pressure (SLP), surface wind, and SAT defined on a $2.5° \times 2.5°$ global grid from 1979 to 2008 inclusive. The fields were generated by the reanalysis (version 1) carried out by the National Centers for Environmental Prediction (NCEP; and were downloaded online at http://www.esrl.noaa.gov/psd/).

The bivariate MJO index of WH04 (downloaded online at http://www.cawcr.gov.au/) is based on the first two empirical orthogonal functions of outgoing longwave radiation and 850- and 200-hPa zonal winds. The annual cycle and interannual variability were removed before the empirical orthogonal function analysis was performed (see WH04 for details). The two components of the bivariate MJO index will henceforth be denoted by x_1 and x_2 and the instantaneous amplitude by $A = \sqrt{x_1^2 + x_2^2}$. Time series plots of x_1 and x_2 (not shown) indicate a quasi-periodic variation of both components with periods between 30 and 80 days (WH04). The two components are approximately in quadrature and their correlation is zero at zero lag (see section 6 for more discussion). The instantaneous phase of the MJO is defined by $\theta = \tan^{-1}(x_2/x_1)$, and is often reported in terms of 8 phases each corresponding to a range in θ of $\pi/4$.

We have used three climatological indices to explore the impact of the background state of the atmosphere and ocean on the response of SAT to the MJO. The
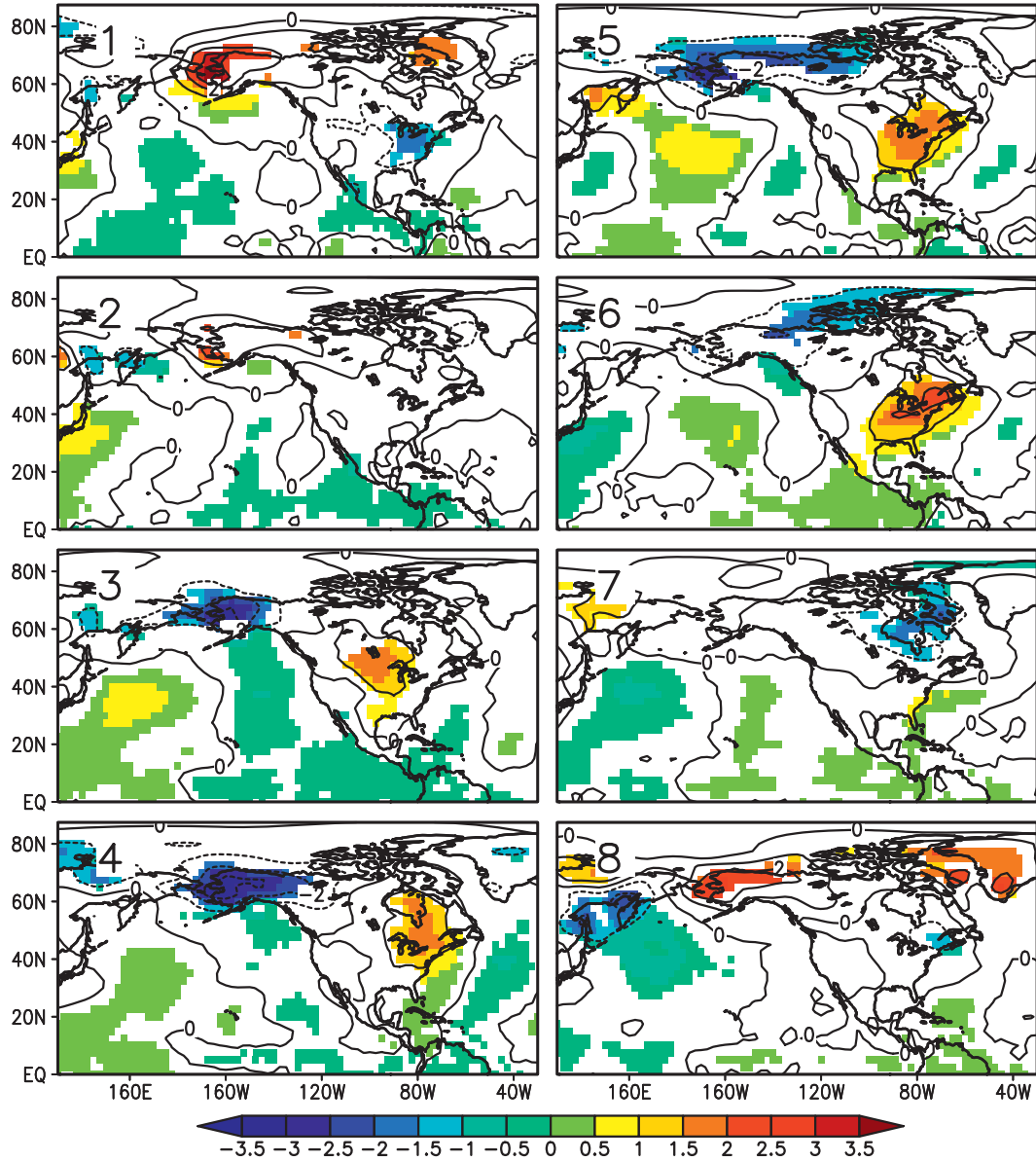
FIG. 1. Composites of observed SAT anomalies for each MJO phase during the boreal winter and $A > 1$. The contour interval is 1°C and the MJO phase is shown in the top-left corner. Shaded areas are different from 0 at the 5% significance level based on Student's t test (e.g., LB09).

PNA was calculated from differences in daily 500-hPa geopotential height from four locations following Wallace and Gutzler (1981). [The AO (e.g., Higgins et al. 2002) was downloaded online at http://www.cpc.ncep.noaa.gov/.] The El Niño/La Niña index is defined as the average of sea surface temperature in the Niño-3.4 region (Trenberth 1997) and was estimated from the National Oceanic and Atmospheric Administration (NOAA) extended reconstructed sea surface temperature analysis (Smith and Reynolds 2003). All three additional indices were obtained for the period 1979 to 2008. The PNA

index is defined daily, and the AO and El Niño/La Niña index are both defined monthly.

The daily reanalysis fields, and the daily PNA and MJO indices, were transformed into 5-day running means resulting in 73 nonoverlapping "pentads" for each of the 30 yr. The monthly AO and El Niño/La Niña indices were linearly interpolated to the central times of the pentads. To emphasize intraseasonal variations, the reanalysis and MJO pentad time series were bandpass filtered to suppress variations with periods shorter than 20 days and longer than 100 days. (A Butterworth filter
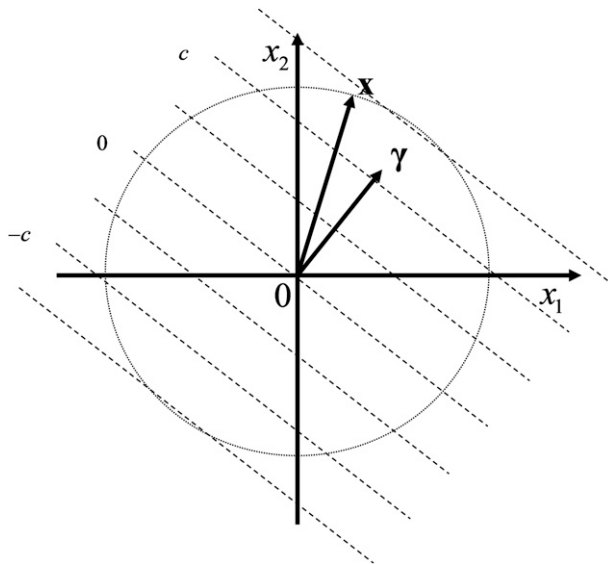
FIG. 2. Schematic showing the dependence of $E(Y) = \gamma_1 A \cos(\theta - \gamma_2)$ on variations of the MJO according to the linear regression model. The coordinates x_1 and x_2 are the components of the bivariate MJO index. The instantaneous state of the MJO is shown by the vector $\mathbf{x}$ (with amplitude A and phase θ). The dashed lines are contours of constant $E(Y)$ and the parameter vector $\boldsymbol{\gamma}$ corresponds to the gradient of this plane. (The $-c$ and c constants indicate a plane of arbitrary gradient passing through the origin.) The dotted line traces out all MJO indices with amplitude A; as the MJO performs a complete cycle with this amplitude $E(Y)$ will vary sinusoidally and reach a maximum when $\theta = \gamma_2$. All of the regression models include an intercept (Table 1), but it has been assumed zero in the schematic.

was used.) The El Niño/La Niña pentad series was low-pass filtered using a Butterworth filter with a cutoff period of 2 yr in order to allow its low-frequency modulating effect on the response of the atmosphere to the MJO to be quantified. For the PNA and AO indices, we tried filtering with different cutoff frequencies (20–100 days, 2 yr) but did not find any significant improvement in model fit.

To explore the seasonal variation of the relationship between the MJO and atmosphere, the observations and indices were stratified by time of year prior to regression analysis. All of the results described in this paper are for boreal winter (defined as December–February inclusive or equivalently pentads 68–73 and 1–12).

b. Traditional compositing of surface air temperature

The SAT-filtered anomalies for boreal winter were conditionally averaged according to the eight phases of the MJO index of WH04. SATs were included in the average only if the MJO amplitude was greater than 1. The number of pentads averaged for each phase ranged

between 23 (phase 1) and 44 (phase 7). For most regions the conditional means are not significantly different from zero based on a standard Student's t test (Fig. 1). Clear exceptions are Alaska, eastern North America, and some regions of the North Pacific. For Alaska there are significant positive (negative) means for phases 1, 2, and 8 (3, 4, and 5); although there are positive (negative) means for phase 7 (6), they are not significantly different from 0. For eastern North America there are significant negative (positive) means for phases 1, 7 and 8 (3, 4, 5, and 6); for phase 2, the mean is negative, but not significantly different from 0.

Overall, the composites shown in Fig. 1 are similar to those presented by VB04 and LB09. In the present study the data were bandpass filtered. By way of contrast, LB09 subtracted the mean of each winter from the pentad data to remove the annual cycle and VB04 subtracted the mean of each boreal winter month from the daily SATs. These differences in data processing presumably account for the slight different between our results and theirs.

3. Compositing through regression modeling

We now describe a modified form of compositing based on the regression of an atmospheric variable of interest (e.g., SAT) on the MJO index. For the linear case the regression model takes the form $E(Y) = \beta_1 x_1 + \beta_2 x_2$ where $E(Y)$ denotes the expected value of SAT as a function of the MJO. This model can be written, without loss of generality, as

$$E(Y) = \gamma_1 A \cos(\theta - \gamma_2), \tag{1}$$

where $\gamma_1 = \sqrt{\beta_1^2 + \beta_2^2}$ scales the instantaneous amplitude of the MJO and $\gamma_2 = \tan^{-1}(\beta_2/\beta_1)$ shifts its phase. According to Eq. (1) the expected response is proportional to the projection of the MJO index onto the two-dimensional vector $\boldsymbol{\gamma}$ that determines the linear response of SAT to the MJO at a given location (see Fig. 2). This approach is similar to that of Ropelewski and Halpert (1986), who used harmonic dial vectors to quantify the influence of ENSO on North American precipitation and temperature based on a constant ENSO period of 24 months.

To use Eq. (1) to generate the equivalent of a sequence of composites (e.g., Fig. 1) we fit it to observations of SAT for each grid point taken from a grid covering the region of interest. From the estimates of γ_1 and γ_2, it is then possible to estimate the expected response for a given MJO phase (with the amplitude fixed) for each grid point and then contour the estimates across the grid (e.g., Fig. 3). In contrast to traditional compositing (see section 2) the regression approach
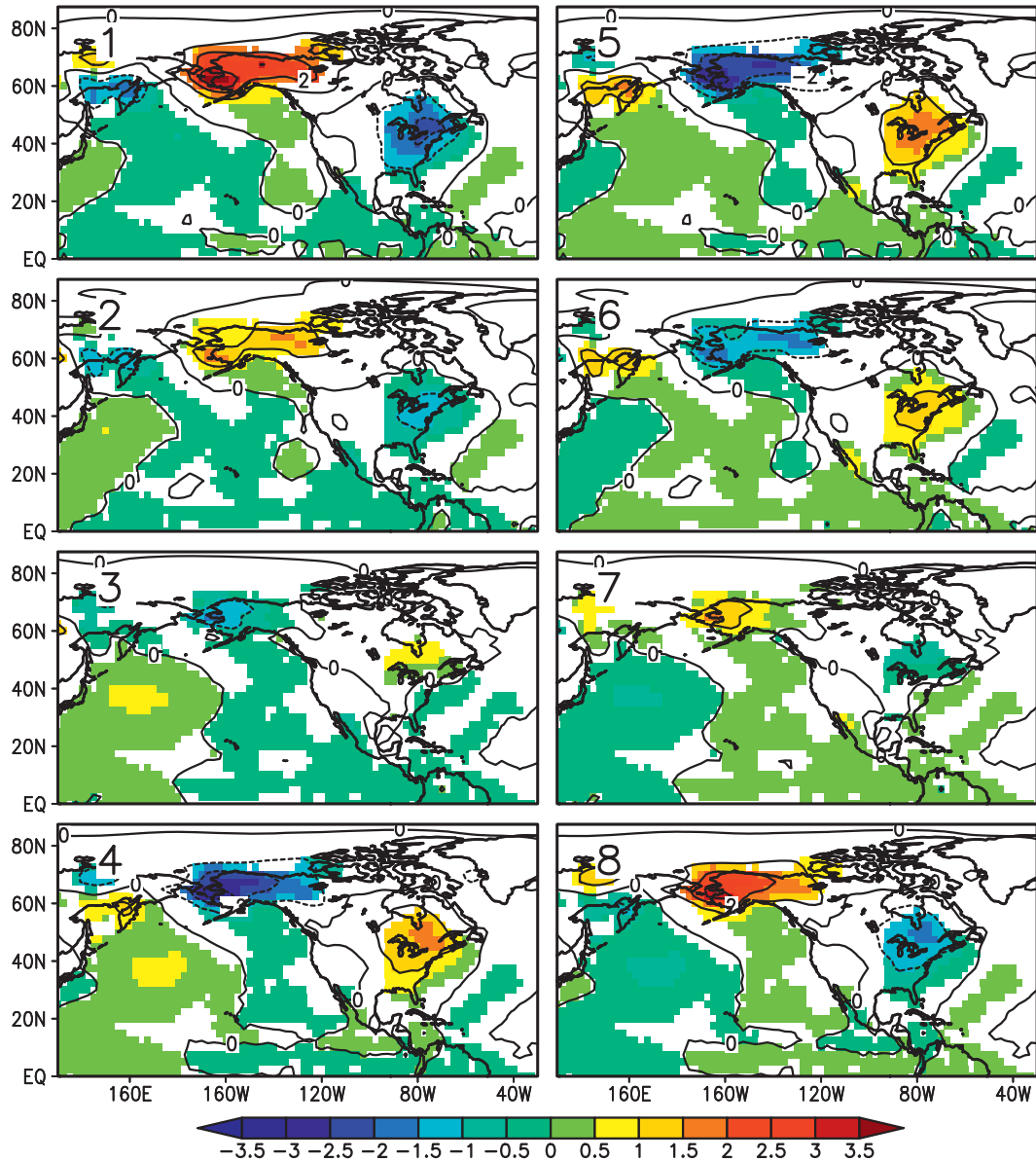
FIG. 3. SAT anomalies as a function of MJO phase during the boreal winter according to the linear regression model. The contour interval is 1°C. The magnitude of the MJO was assumed equal to its mean value ($A = 1.08$, see dotted line in Fig. 2). Shaded areas are significant at the 5% level (see appendix B).

provides estimates of the mean response for a given phase by fitting the model to observations from all phases; it also constrains the estimates to be sinusoidal with respect to MJO phase. Note that the regression approach does not impose any spatial structure on the response.

In general, $\boldsymbol{\gamma}$ will change with location. A map of γ_1 will show the amplitude of the sinusoidal response of $E(Y)$ to a complete cycle of the MJO (see dotted line in Fig. 2); a map of γ_2 will show the MJO phase at which $E(Y)$ is maximum ($\theta = \gamma_2$). These coamplitude and cophase maps are therefore useful in identifying regions

where the MJO response is large, and possibly "standing" (phase constant or different by π) or "propagating" (phase increases smoothly with position). Such maps are similar to the cotidal and cophase maps that have been used for many years to display tidal variations of sea level (e.g., Proudman and Doodson 1924). Note that a major advantage of their use in MJO research is the replacement of a sequence of composites by just two maps. Examples will be given in the next section.

One of the advantages of the above linear model is that it can be readily extended to accommodate

TABLE 1. Main classes of the linear and nonlinear regression models used in this study. The models are all of the form $E(Y_i) = \gamma_0 + \Phi_{1i}(\boldsymbol{\gamma}_1)A_i \cos[\theta_i - \Phi_{2i}(\boldsymbol{\gamma}_2)]$, where $\boldsymbol{\gamma}_1$ and $\boldsymbol{\gamma}_2$ are vectors, $A_i = \sqrt{x_{1i}^2 + x_{2i}^2}$ is the instantaneous amplitude of the MJO index, and $\theta_i = \tan^{-1}(x_{2i}/x_{1i})$ is the corresponding phase for time step i. The factors $\Phi_{1i}(\boldsymbol{\gamma}_1)$ and $\Phi_{2i}(\boldsymbol{\gamma}_2)$ allow the amplitude and phase of the mean response to change with the amplitude of the MJO and the additional index/indicator variable I.

Model	$\Phi_{1i}(\boldsymbol{\gamma}_1)$	$\Phi_{2i}(\boldsymbol{\gamma}_2)$
M_1	γ_1	γ_2
M_2	$\gamma_1 + \gamma_3 I_i$	$\gamma_2 + \gamma_4 I_i$
M_3	$\gamma_1 + \gamma_3 A_i$	$\gamma_2 + \gamma_4 A_i$

nonlinear relationships. For example, it is possible to replace γ_1 in Eq. (1) by terms of the form $\gamma_1 + \gamma_3 A$ thereby allowing $E(Y)$ to increase quadratically with MJO amplitude (e.g., Roundy and Frank 2004a,b). Similarly, the phase lag γ_2 could also vary with A. Two classes of nonlinear models (M_2 and M_3) are defined in Table 1. The form of these nonlinear models involved some "trial and error." In this study, we found that the use of quadratic and high-power terms in A to replace γ_1 and γ_2 was not particularly useful in extratropical regions.

Another straightforward way to extend the linear model is to allow γ_1 and γ_2 to depend on the background state of the atmosphere or ocean as measured by a slowly varying index like the PNA, AO, and El Niño/ La Niña (model M_2; Table 1). We found that the use of such modulating indices in the regression model led to a significant improvement in model fit in some regions. Details are provided in the next section.

To quantify the fit of the regression model we have used the coefficient of determination (R^2), which corresponds to the squared correlation between the model predictions and the observations of the variable of interest. The justification for using R^2 to quantify the fit of the nonlinear models is given in appendix A. To assess the statistical significance of the fit it is necessary to take into account possible autocorrelation of the observations (e.g., Johnson and Wichern 2007). Our approach is very pragmatic and is based on Monte Carlo techniques that lead to approximate p values. Details are given in appendix B.

4. Extratropical SAT and the MJO

We now map the variation of SAT related to the MJO using the methodology described in the previous section. In the first subsection we describe results from the linear regression model M_1 and present global maps of coamplitude and cophase (section 3). In section 4b results from the nonlinear regression models are evaluated
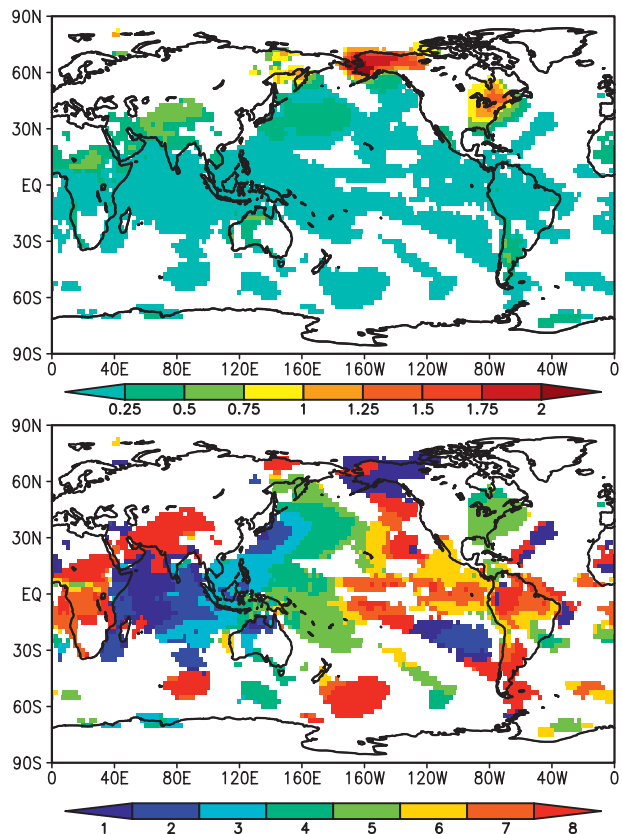

FIG. 4. Coamplitude and cophase maps of SAT during boreal winter calculated using the linear regression model. (top) Coamplitude map based on γ_1. (bottom) Cophase map based on γ_2 (converted to phase of the MJO). See text for details. Shaded areas are significant at the 5% level (see appendix B).

with a particular focus on model M_2. The strongest SAT response is found over North America and this signal is described in more detail in section 4c.

a. Results from the linear model

Predictions of SAT calculated using the linear regression model are shown in Fig. 3. The format (e.g., domain, MJO phase) was chosen to coincide with the sequence of composites shown in Fig. 1. Note the amplitude of the MJO was set to its mean value ($A = 1.08$, dotted line of Fig. 2). The color shaded areas are significant at the 5% level based on the "cloning" method described in appendix B.

Overall there is reasonable agreement between the variations of SAT shown in Figs. 1 and 3 including the amplified response over Alaska and eastern North America. The timing of the maximum in these regions is also quite similar. There are, however, some significant differences between the two figures. In general the temporal variations of the regression predictions (Fig. 3)

are smoother than those from traditional compositing (Fig. 1). The reason is that the maps of Fig. 3 are based on a model that (i) is constrained to vary sinusoidally with MJO phase at each grid point, and (ii) is fit to all 540 pentad values. By way of contrast, the panels in Fig. 1 are each based on less than 44 pentads (see section 2) and are not constrained to change smoothly with phase. Another noticeable difference is that the maps from the regression model are spatially smoother than the traditional composites. We argue that this results from the observations (or more precisely, the "signal" as opposed to "noise" component of the observations), because the fitting procedure does not impose any spatial structure on the model predictions. (All of the models, including M_1, are fit independently to time series of observations from each grid point.)

As discussed in section 2 it is possible to use the linear regression model to provide a parsimonious description of the covariation of extratropical SAT with the MJO using coamplitude and cophase maps. Figure 4 shows the global distribution of γ_1 and the corresponding phase map. The shaded areas of Figs. 4 and 3 coincide and correspond to model fits that are significant at the 5% level (see appendix B). It is clear from the coamplitude map that γ_1 is largest over Alaska and eastern North America. In the tropics, γ_1 is significantly different from zero but of smaller amplitude; this is due to the lower background noise in this region (see discussion of R^2 later in this section). The bottom panel of Fig. 4 shows the phase lag of SAT with respect to the MJO (i.e., γ_2, the MJO phase for which local SAT is maximum). In the tropics, from the Indian Ocean to South America, the phase increases smoothly indicating an eastward-propagating SAT signal. From Japan to Alaska the phase indicates a northeastward-propagating, extratropical SAT signal. There is a similar extratropical signal in the Southern Hemisphere propagating from Australia to South America.

It is important to note that the information conveyed by Figs. 3 and 4 is essentially identical because both are based on M_1. The coamplitude/cophase maps, however, provide a more parsimonious description (only two maps are required) and are useful in identifying standing and propagating patterns of SAT response.

The fit of the linear model M_1 is indicated by the map of R^2 shown in the top panel of Fig. 5. The model generally fits best in the vicinity of the winter intertropical convergence zone (ITCZ; see, e.g., Kiladis and Weickmann 1992a) with local maxima over the Maritime Continent, West Africa, and Peru where $R^2 \approx 0.3$. There is also evidence of an extratropical limb of elevated R^2 in the Northern Hemisphere that starts near the Maritime Continent and corresponds to signals propagating to the
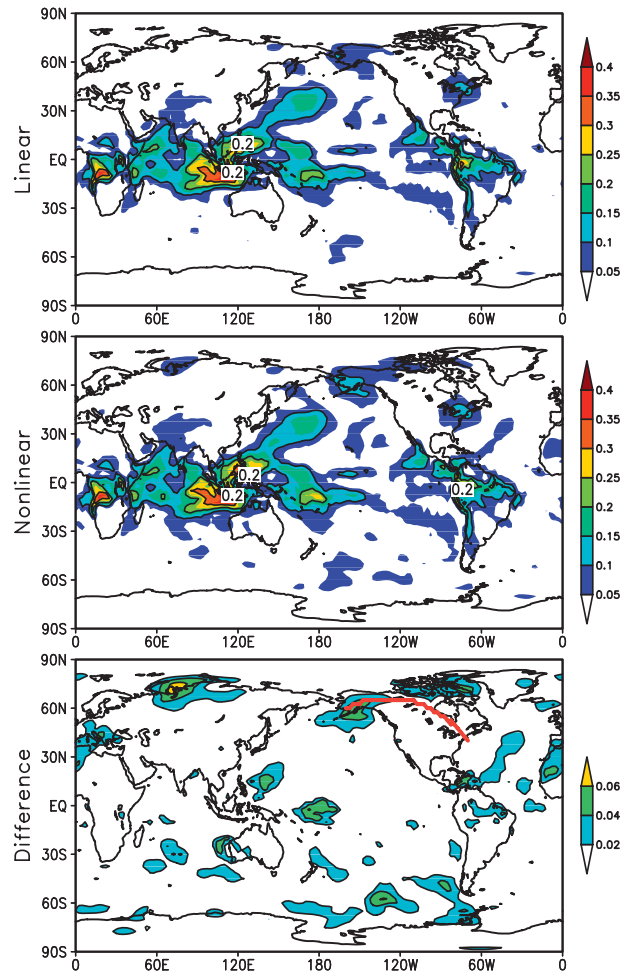

FIG. 5. Fit of (top) the linear regression model and (middle) the nonlinear regression model M_2. Fit is measured by the R^2 statistic. (bottom) The difference between (top) and (middle). The contour interval is 0.1 for (top) and (midde) and the shaded areas correspond to $R^2 \geq 0.05$. The contour interval is 0.02 for (bottom) and the shaded areas correspond to $R^2 \geq 0.02$. The red line in (bottom) is used in Fig. 6.

northeast (mentioned earlier in relation to the cophase map). Relatively high values of R^2 of around 0.1 (corresponding to correlations of about 0.3) are also found over Alaska and eastern North America.

b. Results from the nonlinear models

The nonlinear models used in this study are a straightforward extension of Eq. (1) and involve generalizing the amplitude factor γ_1 and phase lag γ_2 to depend on the MJO amplitude and low-pass-filtered indices (I, see section 2). The nonlinear model for the ith SAT observation takes the following form:

$$E(Y_i) = \gamma_0 + \Phi_{1i}(\boldsymbol{\gamma}_1)A_i \cos[\theta_i - \Phi_{2i}(\boldsymbol{\gamma}_2)], \qquad (2)$$
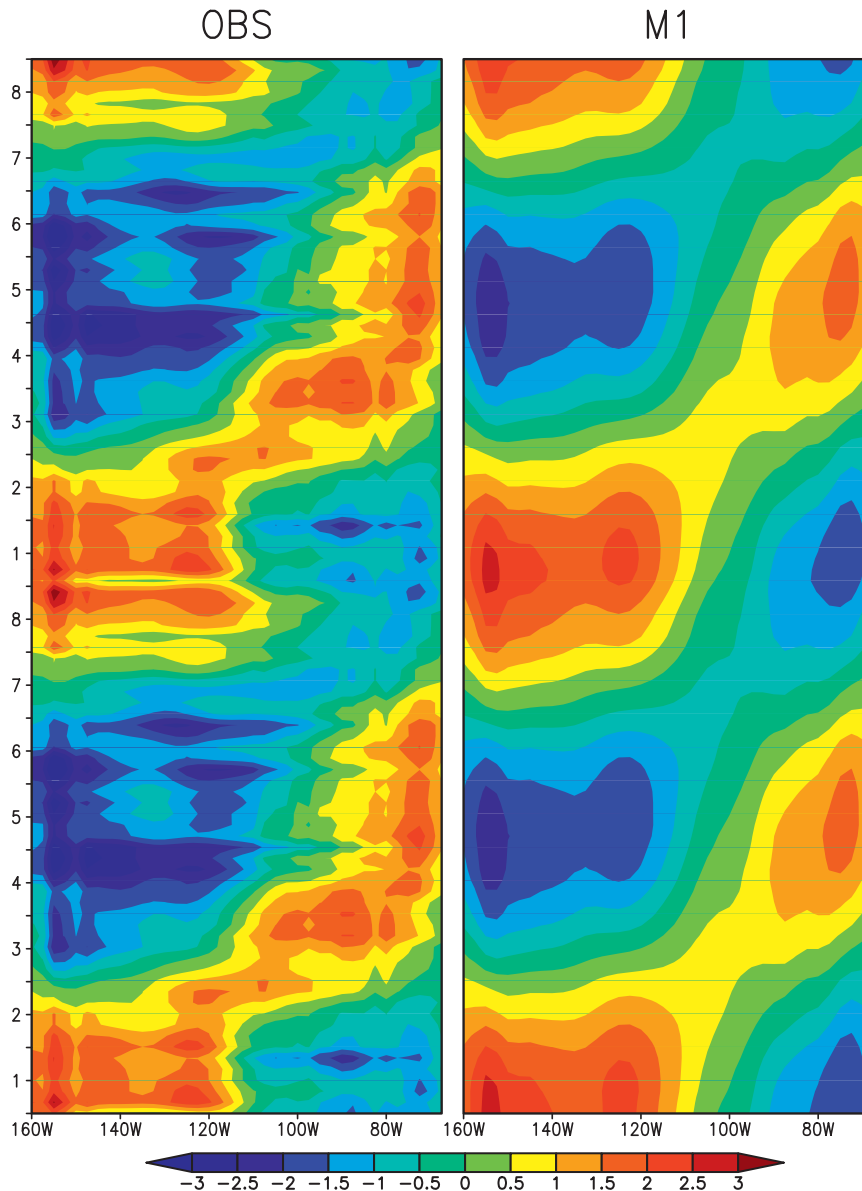
OBS M1

FIG. 6. Variation of North American winter SAT with MJO phase. The x axis defines the position along the red line shown in Fig. 5 (bottom). The y axis defines MJO phase over two cycles. (left) Composites of observed winter SAT anomaly, conditionally averaged by MJO phase for $A > 1$. The composites were smoothed with a running average of width $2\pi/8$ (corresponding to one MJO phase, see text for details). (right) Predictions from the linear model M_1 with MJO amplitude equal to its mean ($A = 1.08$).

where $\boldsymbol{\gamma}_1$ and $\boldsymbol{\gamma}_2$ are now vectors. For the linear model $\Phi_{1i}(\boldsymbol{\gamma}_1) = \boldsymbol{\gamma}_1$ and $\Phi_{2i}(\boldsymbol{\gamma}_2) = \boldsymbol{\gamma}_2$.

The two classes of nonlinear model used in this study are described in Table 1. They allow for the dependence of the amplitude and phase of the response on the amplitude of the MJO and index/indicator variables denoted by I. In this study, I is either an index (such as the intensity of La Niña) or an indicator variable (e.g., Bates and Watts 1988) derived from an index (e.g., $I = 1$

if the index exceeds a specified threshold, and 0 otherwise). More complex models, involving sums of products of powers of A_i and I_i were tried but are not listed in this table. The best results (high R^2, small number of parameters) were obtained by a trial and error and corresponded to M_2 with $\gamma_4 = 0$ and an indicator variable I_i that equaled one if the El Niño/La Niña index was less than -0.4, and 0 otherwise. The threshold value of -0.4 was chosen to ensure a relatively large
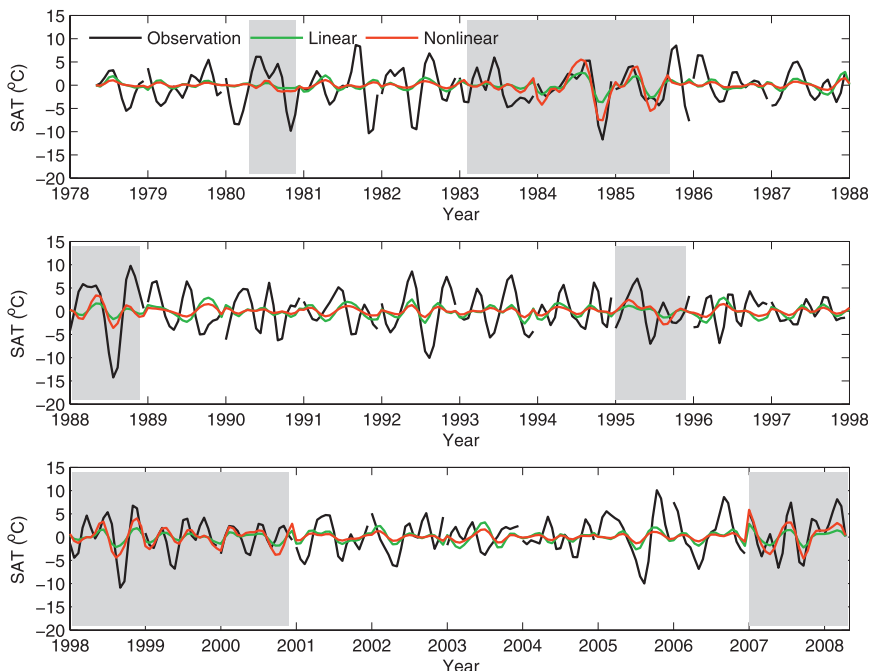
FIG. 7. Time series of observed (black curves) winter SAT for Alaska and predictions from the linear (green curves) and nonlinear (red curves) models. The tick marks on the x axis denote boreal winters (December–February inclusive). The y axis corresponds to the SAT anomaly averaged over 57.5°–70°N, 160°–142.5°W. The shaded areas are years when El Niño/La Niña index is less than −0.4. (top) 1979–88, (middle) 1988–98, and (bottom) 1998–2008. A short break has been added to indicate the transition from one winter to the next.

sample size of ENSO events (31%), although similar results were obtained by setting the threshold to −0.5 or −0.6. The R^2 maps for M_1 and M_2 are similar (top two panels, Fig. 5) suggesting that the improvement in fit is marginal at best. A more quantitative measure of model improvement is given by the difference in R^2 (bottom panel of Fig. 5). The most impressive improvement in fit for the extratropics was found for Alaska where R^2 increased from about 0.1 to 0.15. This region is discussed in more detail in section 4c.

c. SAT from Alaska to eastern North America

The variation of SAT as a function of MJO phase and position is shown in Fig. 6. The left panel shows observed SAT anomalies averaged according to MJO phase ($A > 1$). The figure was obtained by dividing the MJO cycle into 48 divisions and then applying a running average across the composites for each division. The running average was over one phase of the MJO (equivalently to averaging over 6 divisions). The sample size for each phase of the MJO ranged from 18 to 44 pentads. The SAT peaks first in Alaska over a broad range of phases centered on phase 1. Between phases 2 and 4 there is evidence of eastward propagation, and weakening, of the Alaskan signal to about 80°W (southern

Quebec). Between phases 4 and 6 there is an amplified peak in SAT over the eastern coast of North America that is out of phase with the contemporaneous SAT in Alaska. The right panel shows the corresponding prediction from the linear model M_1. The model prediction is generally similar to the observed means (left panel). According to the nonlinear model there is an enhanced response in Alaska during La Niña years (figure not shown).

To obtain a more detailed picture of the observed SAT variations for Alaska, and the corresponding model predictions, their time series are shown in Fig. 7. The linear predictions (green curves) range from −3.7° to 3.2°C and their correlation with the observations (black curves) is 0.28, consistent with squared correlations plotted in the top panel of Fig. 5. The nonlinear predictions (red curves) range from −7.5° to 5.9°C and their correlation with the observations (black curves) is 0.35 (middle panel, Fig. 5). If we restrict the nonlinear predictions to times when the El Niño/La Niña index is less than −0.4 (shaded regions) their correlation with the observations increases to 0.54. Note the nonlinear model fits particularly well during strong La Niña years (El Niño/La Niña index less than −0.6 corresponding to years 1984/85, 1988/89, 1998/99, 1999/2000, and 2007/08).
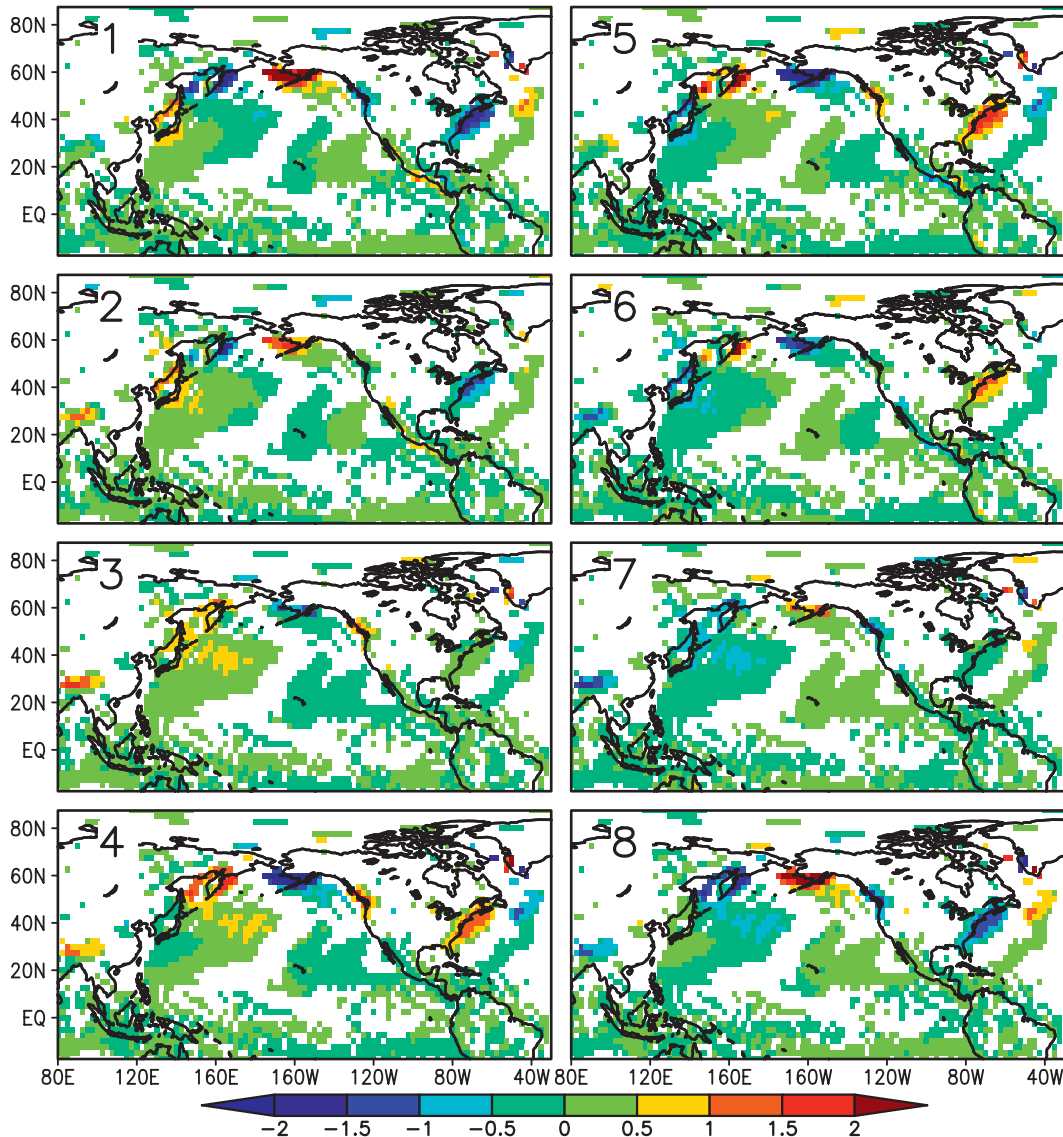
FIG. 8. As in Fig. 3, but for horizontal advection $-\mathbf{V} \cdot \mathbf{V}T$ in °C day^{-1}. (See text for details.)

The correlation during El Niño events is 0.23. MJO convection is shifted about 20° eastward during El Niño events (Hendon et al. 1999; Kessler 2001; WH04). This could potentially alter the wave response to MJO convection, as discussed for example in the context of the seasonal cycle by Winkler et al. (2001).

5. Physical interpretation

Alaska and the adjacent ocean is known to be a region with strong gradients in SAT during boreal winter (due to extreme land–sea contrasts). This led VB04 to speculate that horizontal advection could be used to explain the relationship between SAT and the MJO in this region.

Motivated by VB04, we first checked if there was a relationship between winter SAT and local surface wind in the vicinity of Alaska and the east coast of North America. The correlation between local shore-normal wind and SAT was 0.84 and 0.63 for Alaska and the East Coast of North America, respectively. ("Shore normal" was defined based on the local orientation of the coastline.) Encouraged by these results we next calculated, for each grid point a time series of daily SAT advection ($-\mathbf{V} \cdot \mathbf{V}T$), where $\mathbf{V}T$ is the local gradient of SAT, and $\mathbf{V}$ is the local surface wind. After bandpass filtering (cutoff periods of 20 and 100 days, see section 2) the linear model M_1 was fit to the advection time series for each grid point and the response plotted as a function of MJO phase (Fig. 8). There is clearly strong similarity between
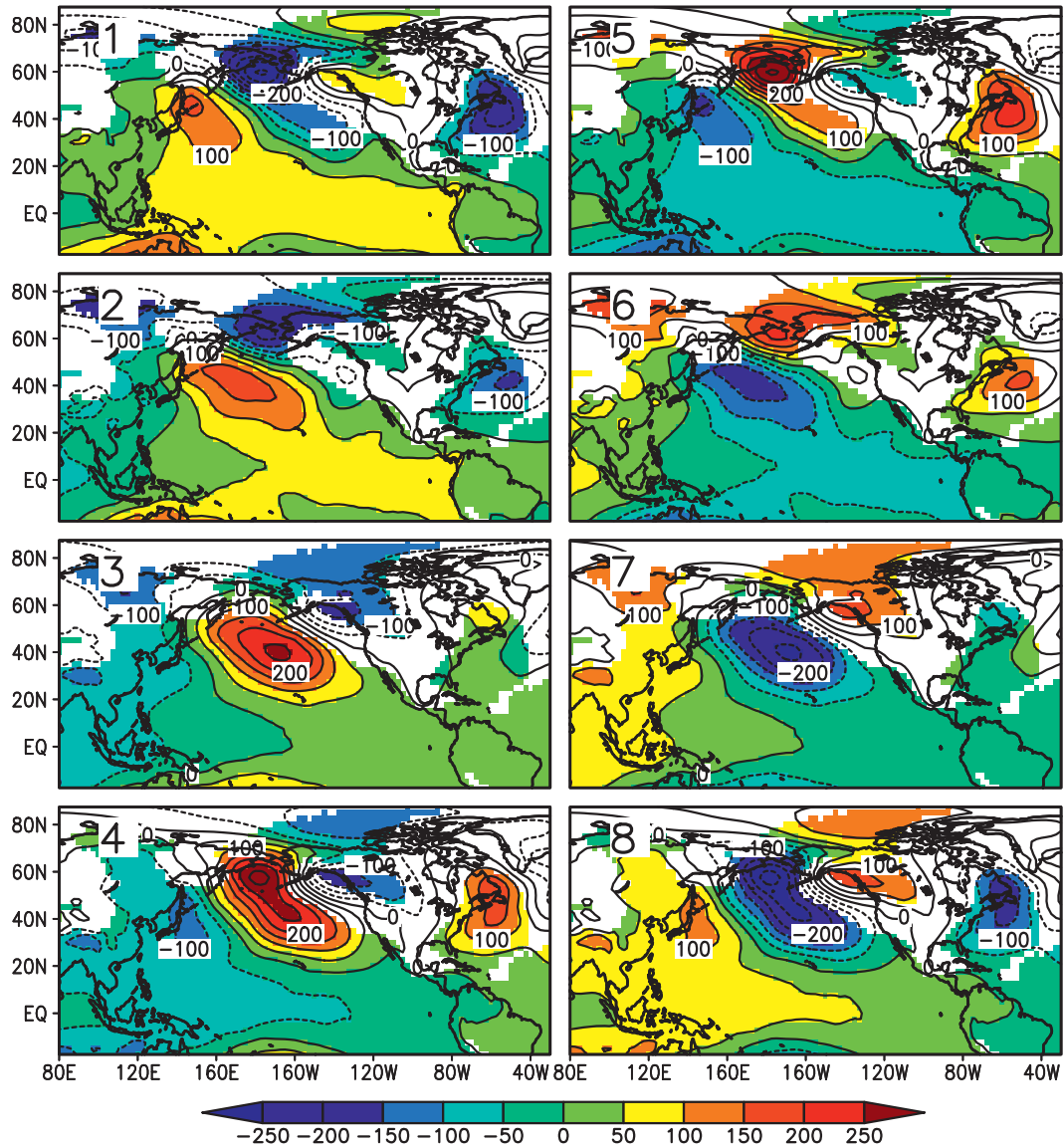
FIG. 9. As in Fig. 3, but for SLP in Pa.

Fig. 8 (allowing for a phase lag of approximately one-quarter of a cycle) and Figs. 1 and 3. This leads us to conclude that SAT variations over Alaska and eastern North America are due primarily to horizontal SAT advection.

To relate the local shore-normal wind to the larger-scale, surface atmospheric circulation we next used the linear regression model to map SLP as a function of MJO phase (Fig. 9). During phases 1, 2, 7, and 8 (3, 4, 5, and 6), there is a negative (positive) SLP anomaly to the west of Alaska that is associated with an onshore (offshore) wind anomaly that advects warm (cold) air consistent with Figs. 1 and 3. The same mechanism can be used to explain the SAT variations on the east coast of North America.

In the tropics, SLP anomalies can be clearly identified propagating from west to east over an MJO cycle (Fig. 9). The SLP anomalies near Alaska and east coast of North America can be traced back to low latitudes, consistent with the teleconnection mechanism associated with Rossby wave propagation (Wallace and Gutzler 1981; Weickmann et al. 1985; Murakami 1988). To show this we generated maps of geopotential height anomaly at 500 hPa (H_{500}) as a function of MJO phase using the same linear approach as before (Figs. 10 and 11). In the tropics we can clearly identify anomalies that propagate from west to east over an MJO cycle as expected. The teleconnection of anomalies in midlatitudes to the tropics is clearly evident in the regular sequence of cells that can
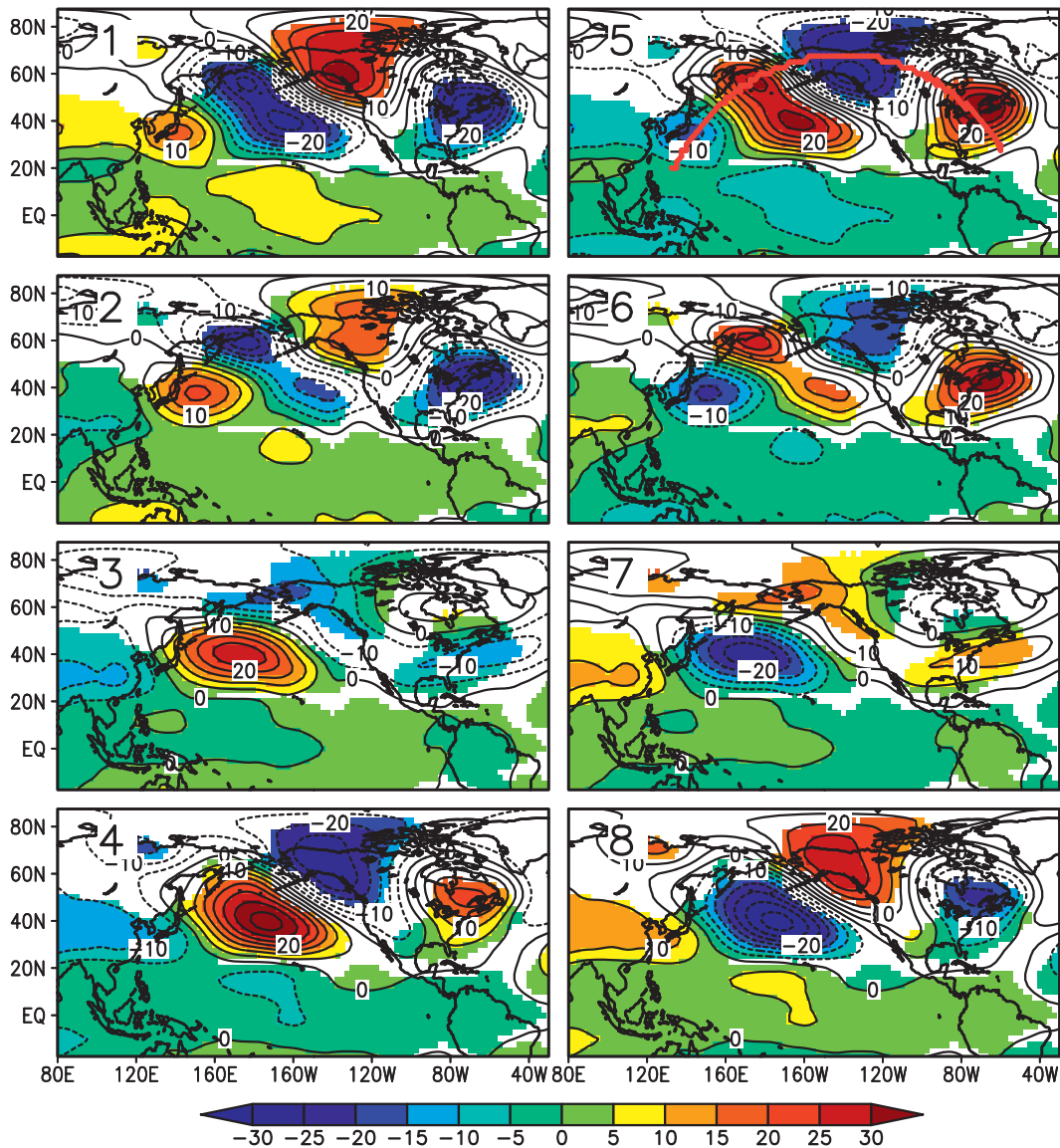
FIG. 10. As in Fig. 3, but for geopotential height anomaly of the 500 hPa surface (in gpm). (top) The red line is used in Fig. 11.

be seen propagating along the line defined in the top-right panel of Fig. 10. [This chain of cells is reminiscent of the features propagating along a great circle calculated by Hoskins and Karoly (1981) using linear theory.] The patterns at 500 hPa are similar to those at 200 hPa shown by Kiladis and Weickmann (1992b). Figures 10 and 11 allow one to trace the propagation of a H_{500} anomaly from southern Japan (phase 8), across the North Pacific (phase 5) after which it weakens before being amplified near Alaska (phase 8). The same anomaly can continue to be traced into the second MJO cycle as it propagates southeastward across North America before being reamplified near the east coast and then

disappearing over the North Atlantic. It is perhaps worth emphasizing that although the variations at a fixed location in Figs. 10 and 11 are sinusoidal in MJO phase, and repeat exactly over one MJO cycle, it is possible to track specific features for more than one cycle (see Fig. 11).

Traditional compositing has the potential to reveal more detail than the approach advocated here because it can includes information on the higher harmonics of the fundamental MJO period. This increases the degrees of freedom of the predicted fields, but also means that these fields are subject to greater estimation error; the problem is particularly acute when the length of
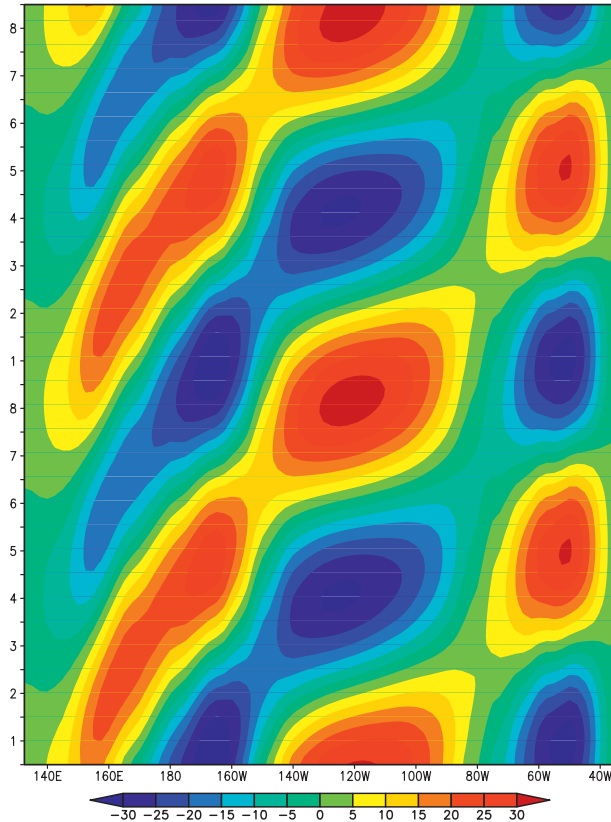
FIG. 11. Geopotential height anomaly of the 500-hPa surface (in gpm) as a function of MJO phase according to the linear model M_1. The format is the same as Fig. 6. The x axis defines position along the red line shown in Fig. 10 (top right).

the observed records is short. In our approach, M_1 is fit only to the fundamental harmonic.

6. Discussion

The relationship between surface air temperature and the MJO has been explored using a regression based approach. The linear regression model leads directly to maps of coamplitude and cophase for SAT that are similar to the cotidal and cophase maps used for many years by oceanographers to chart tidal variations at a given frequency. The reason the coamplitude and cophase maps are straightforward to interpret is that the two MJO indices (x_1 and x_2) are approximately equal up to a Hilbert transform and the phase of the MJO is approximately proportional to time ($\theta \approx \omega_0 t$, where ω_0 is the dominant frequency of the band-passed MJO). Thus, the linear regression on x_1 and x_2 is similar to regressing SAT on $\cos(\omega_0 t)$ and $\sin(\omega_0 t)$ over a sliding time window and, in this sense, is similar to tidal analysis.

The linear model was extended to allow for nonlinearity in both the parameters and predictor variables.

The statistical significance of the model fits was assessed using a pragmatic Monte Carlo–based technique that allowed for autocorrelation. As in previous studies, no allowance was made for multiple testing models for different grid points and so the statistical significance of the fits is overestimated.

Maps of North American SAT as a function of MJO phase were calculated using conventional compositing and the linear regression approach. Although the results were found to be broadly similar there are some important differences: the results from the regression model are smoother in space and time, and easier to interpret, than the composites. The reason is the regression model constrains the variation of SAT with MJO phase and this reduces the number of parameters to be estimated. In fact only two parameters are needed for each grid point for the linear model in contrast to conventional compositing, which requires eight, one for each MJO phase. In effect compositing has more flexibility to fit the data, but this can lead to unacceptably high sampling variability when the records are short and the signals are weak (the situation we encountered in this study).

Global coamplitude and cophase maps of the covariation of SAT and the MJO were presented for the first time in this study. Eastward-propagating signals in winter SAT can be clearly identified along the equator. Although the fits are generally weak in the extra tropics, the signature of SAT signals propagating poleward from the tropics can be identified in both hemispheres. The strongest extratropical signals are over North America, particularly Alaska and eastern North America (consistent with previous studies e.g., VB04; LB09.)

Our physical explanation of the amplified SAT response for Alaska is that it is due to horizontal advection by shore-normal winds blowing across the strong SAT gradient that exists in this region in winter. By calculating coamplitude and cophase maps for SLP and H_{500}, we were able to link shore-normal wind variations to a chain of propagating height cells that originate in the tropics. Thus, the reason for the warm SAT in Alaska during MJO phases 1 and 8 is the coincidence of a strong SAT gradient coupled with onshore surface winds strongly linked to the MJO. There is evidence in the cophase maps that the SAT signal generated over Alaska moves eastward over North American before being amplified again in the vicinity of Cape Cod by essentially the same mechanism (i.e., horizontal advection by shore-normal winds). The result is that the variations of SAT from Alaska and the east coast are out of phase.

Following previous studies we explored the impact of El Niño and La Niña on the covariation of the atmosphere

and MJO. We found that the SAT predictions are stronger during La Niña years, and that both linear and nonlinear predictions are more accurate during such periods. The difference identified here is consistent with the analysis of Tam and Lau (2005) who explored related dynamic processes including wave activity and propagation, and also circulation patterns. During El Niño events, MJO convection is shifted about 20° eastward past the date line (Hendon et al. 1999; Kessler 2001; WH04). This potentially alters the wave response, consistent with the suggestion of Winkler et al. (2001). In practical terms this means that there is significantly more predictability in Alaskan SAT during La Niña years due to the MJO.

In summary, we have introduced some new tools for mapping the dependence of the atmosphere on the MJO and used them to gain some insight into the underlying physics, focusing on the North Pacific and North America. There is clearly a need to complement this type of empirical study with atmospheric general circulation model simulations if the true physical mechanisms are to be better understood. There are several interesting questions that we plan to pursue in future modeling studies including why does the MJO signal in geopotential height amplify in the vicinity of Alaska?

APPENDIX A

Quantifying Model Fit

The models defined in Table 1 are all of the following form:

$$\hat{y}_i = \gamma_0 + (\boldsymbol{\gamma}_1^T \mathbf{a}_i) f_i(\boldsymbol{\gamma}_2^T \mathbf{b}_i), \qquad \text{(A1)}$$

where subscript i refers to the ith observation. In terms of the models listed in Table 1 the scalar factor $(\boldsymbol{\gamma}_1^T \mathbf{a}_i)$ corresponds to the amplitude of the response to MJO forcing. According to Eq. (A1) this amplitude can depend linearly on an arbitrary number of time varying factors stored in the column vector $\mathbf{a}_i$. The function $f_i(\boldsymbol{\gamma}_2^T \mathbf{b}_i)$ allows for nonlinear dependence of the atmospheric variable interest on other factors stored in the column vector $\mathbf{b}_i$. To illustrate, for model M_1, $\boldsymbol{\gamma}_2$ is a scalar, $\mathbf{b}_i = 1$, and $f_i = \cos(\theta - \gamma_2)$.

To estimate γ_0, $\boldsymbol{\gamma}_1$, and $\boldsymbol{\gamma}_2$, we minimize the following sum of squares of errors:

$$J(\gamma_0, \boldsymbol{\gamma}_1, \boldsymbol{\gamma}_2) = \sum_{i=1}^{n} (y_i - \hat{y}_i)^2. \qquad \text{(A2)}$$

At the minimum the gradient of J is 0 and this leads to the following conditions:

$$\frac{\partial J}{\partial \gamma_0} = 0 \Rightarrow \sum_{i=1}^{n} (y_i - \hat{y}_i) = 0, \qquad \text{(A3)}$$

$$\frac{\partial J}{\partial \boldsymbol{\gamma}_1} = 0 \Rightarrow \sum_{i=1}^{n} \hat{y}_i (y_i - \hat{y}_i) = 0. \qquad \text{(A4)}$$

Thus, even though Eq. (A1) is possibly nonlinear in $\boldsymbol{\gamma}_2$, the sample mean of the residuals Eq. (A3) and the sample covariance of the residuals and predictions Eq. (A4) are both zero. This means that the sample variance of the observations partitions into a part due to the predictions and a part due to the residuals. (This is not true in general for nonlinear regression models.) For the present class of models we take the variance of the predictions divided by the variance of the observations as the overall measure of model fit:

$$R^2 = \frac{\text{var}(\hat{y}_i)}{\text{var}(y_i)} \quad 0 \le R^2 \le 1. \qquad \text{(A5)}$$

In the linear case, this corresponds to the well-known coefficient of determination.

APPENDIX B

Assessing the Statistical Significance of Model Fit

For data collected over time, observations are often "autocorrelated." In the context of regression modeling this invalidates the use of conventional tests of significance of model predictions and overall fit (e.g., Johnson and Wichern 2007).

Following Oliver and Thompson (2010), we use Monte Carlo techniques to approximate the sampling distribution of R^2 under the assumption of no relationship between the MJO (the independent variables) and the dependent variable of interest. From this sampling

distribution it is then straightforward to obtain p values, and assess the statistical significance of the observed R^2 and thus overall model fit.

We performed the following steps to approximate the sampling distribution of R^2 under the assumption that Y is not related to the MJO: (i) calculate the Fourier transform of the observed Y values, $\{y_i | i = 1, \ldots, n\}$; (ii) randomize the phases of the Fourier transform and then inverse Fourier transform to produce a "clone" of the original series with exactly the same autocovariance structure; (iii) fit the regression model to the clone series and calculate and store R^2; (iv) repeat the last two steps many times and generate the sampling distribution of R^2; and (v) calculate R^2_{obs} from the observed Y values and find the p value (i.e., proportion of R^2 from the clones that exceed R^2_{obs}).

REFERENCES

Bates, D. M., and D. G. Watts, 1988: *Nonlinear Regression Analysis and Its Applications*. Wiley Interscience, 365 pp.

Blade, I., and D. L. Hartmann, 1995: The linear and nonlinear extratropical response of the atmosphere to tropical intraseasonal heating. *J. Atmos. Sci., 52,* 4448–4471.

Camargo, S. J., A. W. Robertson, A. G. Barnston, and M. Ghil, 2008: Clustering of eastern North Pacific tropical cyclone tracks: ENSO and MJO effects. *Geochem. Geophys. Geosyst., 9,* Q06V05, doi:10.1029/2007GC001861.

Cassou, C., 2008: Intraseasonal interaction between the Madden–Julian Oscillation and the North Atlantic Oscillation. *Nature, 455,* 523–527.

Hendon, H. H., C. Zhang, and J. D. Glick, 1999: Interannual variation of the Madden–Julian oscilliation during austral summer. *J. Climate, 12,* 2538–2550.

Higgins, R. W., and W. Shi, 2001: Intercomparison of the principal modes of interannual and intraseasonal variability of the North American Monsoon System. *J. Climate, 14,* 403–417.

——, A. Leetmaa, and V. E. Kousky, 2002: Relationships between climate variability and winter temperature extremes in the United States. *J. Climate, 15,* 1555–1572.

Hoskins, B. J., and D. J. Karoly, 1981: The steady linear response of a spherical atmosphere to thermal and orographic forcing. *J. Atmos. Sci., 38,* 1179–1196.

Jamet, C., and W. W. Hsieh, 2005: Nonlinear atmospheric variability in the winter northeast Pacific associated with the Madden-Julian oscillation. *Geophys. Res. Lett., 32,* L13820, doi:10.1029/2005GL023533.

Jeong, J. H., C. H. Ho, B. M. Kim, and W. T. Kwon, 2005: Influence of the Madden-Julian Oscillation on wintertime surface air temperature and cold surges in East Asia. *J. Geophys. Res., 110,* D11104, doi:10.1029/2004JD005408.

Johnson, R. A., and D. W. Wichern, 2007: *Applied Multivariate Statistical Analysis*. Pearson Education, Inc., 773 pp.

Jones, C., D. E. Waliser, K. M. Lau, and W. Stern, 2004: The Madden–Julian Oscillation and its impact on Northern Hemisphere weather predictability. *Mon. Wea. Rev., 132,* 1462–1471.

Kessler, W. S., 2001: EOF representation of the Madden–Julian oscillation and its connection with ENSO. *J. Climate, 14,* 3055–3061.

——, and R. Kleeman, 2000: Rectification of the Madden–Julian oscillation into the ENSO cycle. *J. Climate, 13,* 3560–3575.

Kiladis, G. N., and K. M. Weickmann, 1992a: Extratropical forcing of tropical Pacific convection during northern winter. *Mon. Wea. Rev., 120,* 1924–1938.

——, and ——, 1992b: Circulation anomalies associated with tropical convection during northern winter. *Mon. Wea. Rev., 120,* 1900–1923.

Kim, J. H., C. H. Ho, H. S. Kim, C. H. Sui, and S. K. Park, 2008: Systematic variation of summertime tropical cyclone activity in the western North Pacific in relation to the Madden–Julian oscillation. *J. Climate, 21,* 1171–1191.

Lau, K. M., and P. H. Chan, 1986: Aspects of the 40–50 day oscillation during the northern summer as inferred from outgoing longwave radiation. *Mon. Wea. Rev., 114,* 1354–1367.

L'Heureux, M. L., and R. W. Higgins, 2008: Boreal winter links between the Madden–Julian oscillation and the Arctic Oscillation. *J. Climate, 21,* 3040–3050.

Lin, H., and G. Brunet, 2009: The influence of the Madden–Julian oscillation on Canadian wintertime surface air temperature. *Mon. Wea. Rev., 137,* 2250–2262.

——, ——, and J. Derome, 2009: An observed connection between the North Atlantic Oscillation and the Madden–Julian oscillation. *J. Climate, 22,* 364–380.

Madden, R. A., and P. R. Julian, 1971: Detection of a 40–50 day oscillation in the zonal wind in the tropical Pacific. *J. Atmos. Sci., 28,* 702–708.

——, and ——, 1972: Description of global-scale circulation cells in the tropics with a 40–50 day period. *J. Atmos. Sci., 29,* 1109–1123.

——, and ——, 1994: Observation of the 40–50-day tropical oscillation—A review. *Mon. Wea. Rev., 122,* 814–837.

McPhaden, M. J., X. Zhang, H. H. Hendon, and M. C. Wheeler, 2006: Large scale dynamics and MJO forcing of ENSO variability. *Geophys. Res. Lett., 33,* L16702, doi:10.1029/2006GL026786.

Mori, M., and M. Watanabe, 2008: The growth and triggering mechanisms of the PNA: A MJO-PNA coherence. *J. Meteor. Soc. Japan, 86,* 213–236.

Murakami, T., 1988: Intraseasonal atmospheric teleconnection patterns during Northern Hemisphere winter. *J. Climate, 1,* 117–131.

Notaro, M., W.-C. Wang, and W. Gong, 2006: Model and observational analysis of the northeast U.S. regional climate and its relationship to the PNA and NAO patterns during early winter. *Mon. Wea. Rev., 134,* 3479–3505.

Oliver, E. C. J., and K. R. Thompson, 2010: Madden-Julian Oscillation and sea level: Local and remote forcing. *J. Geophys. Res., 115,* C01003, doi:10.1029/2009JC005337.

Pan, L. L., and T. Li, 2008: Interactions between the tropical ISO and midlatitude low-frequency flow. *Climate Dyn., 31,* 375–388.

Proudman, J. and A. T. Doodson, 1924: The principal constituent of the tides in the English and Irish Channels. *Philos. Trans. Roy. Soc. London, 231A,* 29–53.

Ropelewski, C. F., and M. S. Halpert, 1986: North American precipitation and temperature patterns associated with the El Niño/Southern Oscillation (ENSO). *Mon. Wea. Rev., 114,* 2352–2362.

Roundy, P. E., and W. M. Frank, 2004a: Applications of a multiple linear regression model to the analysis of relationships between eastward- and westward-moving intraseasonal modes. *J. Atmos. Sci., 61,* 3041–3048.

MONTHLY WEATHER REVIEW

——, and ——, 2004b: Effects of low-frequency wave interactions on intraseasonal oscillations. *J. Atmos. Sci.,* **61,** 3025–3040.

Smith, T. M., and R. W. Reynolds, 2003: Extended reconstruction of global sea surface temperatures based on COADS data (1854–1997). *J. Climate,* **16,** 1495–1510.

Tam, C.-Y., and N.-C. Lau, 2005: The impact of ENSO on atmospheric intraseasonal variability as inferred from observations and GCM simulations. *J. Climate,* **18,** 1902–1924.

Trenberth, K. E., 1997: The definition of El Niño. *Bull. Amer. Meteor. Soc.,* **78,** 2771–2777.

Vecchi, G. A., and N. A. Bond, 2004: The Madden-Julian Oscillation (MJO) and northern high latitude wintertime surface air temperatures. *Geophys. Res. Lett.,* **31,** L04104, doi:10.1029/2003GL018645.

Wallace, J. M., and D. S. Gutzler, 1981: Teleconnections in the geopotential height field during the Northern Hemisphere winter. *Mon. Wea. Rev.,* **109,** 784–812.

Weickmann, K. M., G. R. Lussky, and J. E. Kutzbach, 1985: Intraseasonal (30–60 day) fluctuations of outgoing longwave radiation and 250-mb streamfunction during northern winter. *Mon. Wea. Rev.,* **113,** 941–961.

Wheeler, M. C., and H. H. Hendon, 2004: An all-season real-time multivariate MJO index: Development of an index for monitoring and prediction. *Mon. Wea. Rev.,* **132,** 1917–1932.

Winkler, C. R., M. Newman, and P. D. Sardeshmukh, 2001: A linear model of wintertime low-frequency variability. Part I: Formulation and forecast skill. *J. Climate,* **14,** 4474–4494.

Wu, G., and Y. Zhang, 1998: Tibetan Plateau forcing and the timing of the monsoon onset over South Asia and the South China Sea. *Mon. Wea. Rev.,* **126,** 913–927.

Zhang, C., 2005: Madden-Julian Oscillation. *Rev. Geophys.,* **43,** RG2003, doi:10.1029/2004RG000158.

Zhou, S., and A. J. Miller, 2005: The interaction of the Madden–Julian oscillation and the Arctic Oscillation. *J. Climate,* **18,** 143–159.